

NIST Advanced Manufacturing Series 100-44

**Understanding Anisotropic Tensile
Properties of Laser Powder Bed
Fusion Additive Metals: A Detailed
Review of Select Examples**

Jordan S. Weaver
Idan Rosenthal

This publication is available free of charge from:
<https://doi.org/10.6028/NIST.AMS.100-44>

NIST
National Institute of
Standards and Technology
U.S. Department of Commerce

NIST Advanced Manufacturing Series 100-44

Understanding Anisotropic Tensile Properties of Laser Powder Bed Fusion Additive Metals: A Detailed Review of Select Examples

Jordan S. Weaver
Idan Rosenthal
*Intelligent Systems Division
Engineering Laboratory*

This publication is available free of charge from:
<https://doi.org/10.6028/NIST.AMS.100-44>

November 2021



U.S. Department of Commerce
Gina M. Raimondo, Secretary

National Institute of Standards and Technology
*James K. Olthoff, Performing the Non-Exclusive Functions and Duties of the Under Secretary of Commerce
for Standards and Technology & Director, National Institute of Standards and Technology*

Certain commercial entities, equipment, or materials may be identified in this document in order to describe an experimental procedure or concept adequately. Such identification is not intended to imply recommendation or endorsement by the National Institute of Standards and Technology, nor is it intended to imply that the entities, materials, or equipment are necessarily the best available for the purpose.

**National Institute of Standards and Technology Advanced Manufacturing Series 100-44
Natl. Inst. Stand. Technol. Adv. Man. Ser. 100-44, 30 pages (November 2021)**

**This publication is available free of charge from:
<https://doi.org/10.6028/NIST.AMS.100-44>**

Abstract

There are several physical reasons for anisotropic mechanical properties in additively manufactured metals. These include but are not limited to directionally dependent grain and phase morphology; crystallographic texture; directional porosity/defects; and heterogeneity associated with the melt pool, layer-wise microstructure. All of these are prevalent in most additive manufacturing processes, and it is difficult to separate out the role that each play in the mechanical anisotropy. This review focuses on studies that have attempted to or reasonably isolate one or two of these sources rather than simply report on trends in mechanical properties. This is not an exhaustive review covering all additive process or mechanical properties; the main assessment is on laser powder bed fusion (LPBF) metals and tensile test results (modulus, yield strength, ultimate tensile strength, elongation, and fracture surface analysis).

In summary, the primary sources of anisotropic tensile properties for LPBF alloys are crystallographic texture, anisotropic microstructure morphologies, lack of fusion defects, and the melt pool macrostructure. Within anisotropic microstructures, elongated grains appear to be secondary compared to the preferential distribution of phases and features (e.g., grain boundary alpha, precipitates, etc.). Anisotropic modulus and yield strength are primarily caused by crystallographic texture. This is supported by crystal plasticity simulations. Anisotropic elongation is primarily caused by anisotropic microstructure morphologies, lack of fusion defects, and melt pool macrostructure. The evidence to support this comes from fracture surfaces that follow these features. Melt pool macrostructure is the most challenging to experimentally isolate from the list of other sources of anisotropy. The findings for one set of laser process parameters and alloy are not prescriptive. It's essential that the sources listed above should be characterized before associating the cause of tensile anisotropy to a particular source. Strategies to characterize and manipulate crystallographic texture, porosity, grain and phase morphology, and melt pool macrostructures are required to better understand and control mechanical anisotropy in AM metals.

Key words

Additive Manufacturing; Anisotropy; Laser Powder Bed Fusion; Mechanical Properties.

Table of Contents

1. Standards and Review Articles.	1
1.1. Standards	1
1.2. Reviews	1
2. Main Sources of Anisotropic Tensile Properties	2
2.1. Crystallographic texture	2
2.2. Grain and phase morphology	6
2.2.1. Elongated grains and anisotropic yield strength	6
2.2.2. Microstructure morphology and anisotropic elongation	8
2.3. Lack of fusion defects and anisotropic elongation	11
2.4. Melt pool structure and anisotropic elongation	14
2.5. Residual Stresses	18
3. Summary	18
References	19

List of Tables

Table 1. Anisotropic Young’s modulus, yield stress, and ultimate tensile strength reported by Charmi et al. [17] for 316L stainless steel.	4
Table 2. Anisotropic Young’s yield stress, ultimate tensile strength, and elongation reported by Wang et al. [22] for 316L stainless steel.	6
Table 3. Anisotropic tensile elongation reported by Wilson-Heid et al. [38] for Ti-6Al-4V. Note two different sized tensile specimens were used for pulsed laser (P) and continuous wave laser (CW) samples.	9
Table 4. Anisotropic tensile elongation reported by Ronneberg et al. [55]. Yield stress values are the range of reported values. Elongation is the linear best fit value. Elongation measurements showed significant scatter. The reader is referred to the original reference for more details.	13
Table 5. Anisotropic tensile elongation for LPBF AlSi10Mg reported by Rosenthal et al. [60].	16
Table 6. Summary of tensile anisotropy sources, properties, and micro/macro-structure measurements for LPBF alloys. EBSD – electron backscatter diffraction. EDS – energy dispersive x-ray spectroscopy	19

List of Figures

Fig. 1. (a) 316L stainless steel texture control with discrete changes in laser scan direction along the build height, reused from Ref. [11] under Creative Commons CC BY NC ND license, (b) pure Cr texture control with changes in energy density reused from Ref. [12] under Creative Commons CC-BY license, (c) nickel superalloy 718 texture control with laser power and laser power profile shape reused from Ref. [13] with permission. 3

Fig. 2. elongated grains in the build direction for LPBF (a) high silicon steel reused from Ref. [31] under Creative Commons CC-BY license, and (b) nickel superalloy 625 reused from Ref. [32] with permission..... 8

Fig. 3. Examples of grain boundary alpha highlighted with dotted outlines in (a) Ti-6Al-4V reused from Ref. [40] under Creative Commons Attribution 3.0 license, and (b) post-processed LPBF Ti-6Al-4V-3Fe alloy reused from Ref. [41] under Creative Commons Attribution 4.0 International license. 10

Fig. 4. Lack of fusion defects circled for emphasis for a cross-section of the (a) scan direction (SD) and (b) hatch direction (HD) reused from [55] under Creative Commons CC-BY license. The combination reveals the elongated nature of lack of fusion defects along the scanning direction. 12

Fig. 5. Macrostructure of the SLM AlSi10Mg Alloy: a) Top view revealing the track segment morphology and the 67° rotation of the laser relating to the scan strategy; b) Side view revealing the “fish scale” morphology and the overlapping melt pools. Figures reused from Ref. [59] with permission. 15

Fig. 6. Microstructure morphologies for an AlSi10Mg alloy: a) Melt pool schematic showing the zone locations b) matching microstructure zones: 1 – Coarse fusion zone, 2- Transition zone (referred to as HAZ), 3 – Fine fusion zone. Figures reused from Ref. [59] with permission. 15

Fig. 7. AlSi10Mg fracture surfaces for (a) loading along Z-axis and (b) loading along X-axis reused from Ref. [60] with permission. 17

Fig. 8. Melt pool boundary (MPB) structure and fracture surface schematics for (a) horizontal (X) and (b) vertical (Z) specimens for a uni-directional raster scan strategy in the Y-direction reused from Ref. [58] with permission, (c) horizontal (X/Y) and (b) vertical (Z) specimens for a rotating (67°) scan strategy reused from Ref. [60] with permission..... 18

1. Standards and Review Articles.

1.1. Standards

There are existing standards used for mechanical testing of additive metals. For example, ASTM F3122 – 14 provides a list of ASTM and ISO standards on mechanical properties that are applicable to additive metals [1]. There are also additive manufacturing (AM) specific standards, such as ISO/ASTM52921 – 19, which is a standard that describes the terminology for specimen location and orientation on the build platform [2]. This defines the sample frame (X, Y, and Z axes) so that orientation dependence can be characterized and reported in a consistent manner. In short, the Z axis is aligned with the building direction, the X axis is parallel to the front of the machine and perpendicular to the build direction, and the Y direction is perpendicular to both the Z and X axes. Material specifications for additive metals may list mechanical property requirements in the X, Y, and Z directions separately (e.g., ASTM F3055 - 14a for LPBF IN718 [3]). In the case of laser powder bed fusion (LPBF), the requirements for the X and Y are the same due to the transversely isotropic nature of most LPBF processes that use rotating scan strategies. There are also gaps in standards related to orientation dependent (anisotropic) mechanical properties. The America Makes and ANSI Additive Manufacturing Standardization Collaborative (AMSC) roadmap 2.0 identifies a gap in unique test methods that take into consideration the property inhomogeneity and anisotropy associated with AM parts [4]. A current work item in development since 2015 titled “New Guide for Orientation and Location Dependence Mechanical Properties for Metal Additive Manufacturing” aims to address this gap [5]. Post-process heat treatments can be used to reduce mechanical anisotropy, and their development for this purpose is another gap identified by AMSC Roadmap 2.0 [4]. Developing standards to address the gaps documented in the AMSC 2.0 roadmap requires understanding of the main causes of anisotropic mechanical properties in AM metals. This review focuses specifically on LPBF metals and tensile property anisotropy.

1.2. Reviews

The mechanical properties of additive metals have been reviewed by several authors. An early review by Lewandowski and Seifi in 2016 summarizes a significant amount of tensile property data on Ti-6Al-4V (LPBF, electron beam powder bed fusion (EPBF), and directed energy deposition (DED)) along with some data on other alloys, which is separated by specimen orientation (e.g., Z and X directions) [6]. For Ti-6Al-4V, some studies show similar tensile properties (modulus, strength, ultimate tensile strength (UTS), and elongation) for Z and X directions while others show significant differences in one or all the tensile properties. This suggests that tensile properties of AM metals may be both isotropic and anisotropic. However, the reasons why some studies report nearly isotropic or very anisotropic results is outside the scope of their review. Kok et al. [7] focused a review directly on anisotropic and heterogeneous microstructures and mechanical properties. They provide a summary of anisotropic tensile properties (yield strength and elongation) with a metric that is the difference between X and Z directions normalized by the Z direction for several AM processes and alloys. This anisotropy factor, a percentage, ranges from -9.6% to 41.5% for strength and -471.4% to 84.0% for elongation with some studies reporting less than 1% anisotropy for either property [7]. The review discusses anisotropic microstructures (elongated grains, crystallographic

texture, and lack of fusion defects) broadly as the cause for anisotropic properties, emphasizing elongated grains and texture. In a comprehensive review of process-structure-property relationships in AM metals, Debroy et al. [8] summarize tensile property (yield strength, tensile strength, and elongation) anisotropy with plots of transverse (Z) versus longitudinal properties (X or Y). These plots are grouped by alloys. They find only slight anisotropy for DED and PBF stainless steels and no clear trend in nickel alloys despite the general trend of columnar grains in both material systems. Observations for Ti-6Al-4V suggest there is no strong trend for anisotropy or isotropy and ductility measurements vary significantly compared to conventionally processed alloys. The scatter in ductility is argued to be caused by significant variation in defects. Lastly, they report no notable anisotropy in the strength of Al alloys with anisotropy in elongation (larger elongation for X/Y specimens compared to Z). A discussion of how to distinguish the causes of anisotropy is lacking, which remains important given that several potential causes may exist in any AM metal sample. Distinguishing the relative causes of anisotropy is critical before applying mitigation strategies during processing or post-processing to produce more isotropic materials or in order to take advantage of anisotropy for microstructure sensitive design. Summaries of tensile property trends are extremely useful; however, a review of studies that isolate individual causes of mechanical anisotropy is necessary to better understand the main causes and how to distinguish their relative roles.

2. Main Sources of Anisotropic Tensile Properties

2.1. Crystallographic texture

Crystallographic texture and anisotropy in materials is a mature topic [9, 10]. Polycrystalline materials exist of many individual crystals, each of which has a crystal orientation defined as the passive rotation from the sample frame to the crystal lattice frame. A crystallographic texture exists when specific crystal orientations occur in a higher frequency compared to a random or uniform distribution. Single crystals are inherently anisotropic so when a polycrystalline material has a crystallographic texture, its macroscopic properties take on these anisotropic properties. A texture is characterized by a component (crystal orientation) and its intensity (multiples of a uniform distribution or m.u.d.). Crystals exhibit both elastic and plastic anisotropy and each will be discussed separately. Three examples of LPBF textures and how they change with process parameters are given in Fig. 1. The data in Fig. 1 comes from electron backscatter diffraction (EBSD) measurements and is visualized in grain maps that are color coded based on the crystal plane normal aligned with a specific sample plane (inverse pole figure grain maps) and intensity maps of specific crystal planes with respect to the sample reference frame (pole figures). The three examples in Fig. 1 show (a) manipulation of crystal texture in the X-plane with laser scan strategy [11], (b) crystallographic texture intensity decreasing with decreasing volumetric energy density [12], and (c) manipulation of crystal texture with laser power and power profile shape [13]. DebRoy et al. [8] summarize the texture development process as competitive growth where easy growth crystal orientations aligned with the maximum heat flow outgrow slower, misaligned crystal orientations.

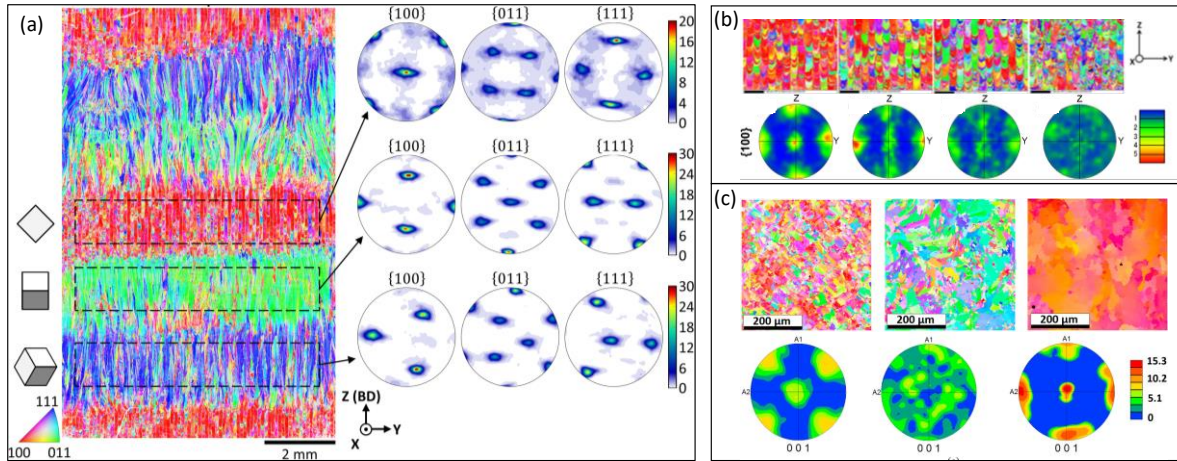


Fig. 1. (a) 316L stainless steel texture control with discrete changes in laser scan direction along the build height, reused from Ref. [11] under Creative Commons CC BY NC ND license, (b) pure Cr texture control with changes in energy density reused from Ref. [12] under Creative Commons CC-BY license, (c) nickel superalloy 718 texture control with laser power and laser power profile shape reused from Ref. [13] with permission.

Textured polycrystalline anisotropy is only possible because of single crystal anisotropy. The relationship between polycrystalline and single crystal elastic anisotropy is well described by Voigt, Ruess, and Hill theories [14-16]. These predictions provide bounds (upper and lower) as well as an expected value. Charmi et al. [17] provide examples of how elastic anisotropy was directly related to crystallographic texture. A summary of the microstructure characteristics and tensile properties is given in Table 1. They built and characterized LPBF 316L with large area electron backscatter diffraction (EBSD) measurements to determine crystallographic texture. The material had a moderate (110) texture (3 m.u.d.) along the build direction. The scan strategy used was an X-Y strategy (90° rotation between layers) with an initial 45° offset. It should be noted that the scan strategy has a significant effect on the texture component and texture intensity (e.g., [18, 19]) so that the texture in Ref. [17] is not representative of all LPBF 316L stainless steel. Furthermore, laser process parameters also greatly influence texture (e.g., a decrease in laser power leading to porosity defects also leads to a less textured and more random orientation distribution [20]). Tensile tests for sample orientations at 0° (X-axis), 45°, and 90° (Z-axis) resulted in Young's moduli of 215 GPa ± 3 GPa, 202 GPa ± 8 GPa, and 192 GPa ± 7 GPa. Various representative volume elements (simulated microstructures) that matched the five texture measurements were used for predictions. For simplification, the representative volume elements (RVEs) contained a single, equiaxed grain size rather than a distribution of grain sizes and shapes. The Hill model and crystal plasticity simulations both matched experimental modulus measurements. Kunze et al. [21] found similar results for a nickel based alloy with a strong (100) texture along the build direction (8 m.u.d): modulus measurements fell inside the Voigt and

Ruess bounds. The main source of elastic anisotropy in AM metals is crystallographic texture. The single crystal elastic anisotropy, the texture component(s), and texture intensity dictate the macroscopic anisotropy. The orientation dependent macroscopic young's modulus can be predicted from available or measured single crystal elastic constants.

Table 1. Anisotropic Young's modulus, yield stress, and ultimate tensile strength reported by Charmi et al. [17] for 316L stainless steel. Modulus values are presumed to be the average \pm one standard deviation from 11 tensile tests.

		Microstructure			
AM Process	Material	Porosity	Grain Morphology	Crystal Texture	Residual Stress
LPBF	316L Stainless Steel	< 0.01%, spherical	Checkerboard in Z plane, some elongated in X and Y Planes	(110) in the Z-axis with an intensity of 3 m.u.d.	-74 MPa to 137 MPa in tensile loading direction
Tensile Properties					
Sample	Modulus (GPa)	Yield (MPa)	UTS (MPa)	Elongation (%)	Fracture Surface
X	215 \pm 3	581	689 to 691	56.5	n/a
45°	202 \pm 8	563 to 564	670 to 671	53.0 to 56.5	n/a
Z	192 \pm 7	506 to 514	611 to 620	53.5 to 59.5	n/a

Crystallographic texture causes plastic anisotropy because plasticity (slip, twinning, phase transformations, etc.) is linked to crystallographic planes. For example, the well-known Schmid's law describes the relationship between the tensile load and the resultant shear stress on a slip system (crystal plane and direction). Plastic slip will occur when the applied shear stress exceeds the slip resistance of the slip system. The shear stress on the slip system (driving force for plastic slip) will depend on its orientation with respect to the tensile axis; thus, there is inherent plastic anisotropy. Further plastic anisotropy occurs when different slip systems have different slip resistances (e.g., hexagonal close-packed (HCP) crystals) and/or other deformation mechanisms have different activation stresses or cause differences in work-hardening when activated (e.g., twinning). The prediction of strength, ultimate tensile strength, and ductility for textured polycrystals is not as trivial as elasticity since it depends on additional microstructural features (e.g., grain size, precipitation hardening, dislocation density, residual stress, etc.). Crystal plasticity models are employed to both predict texture evolution during deformation processes (crystals reorient during deformation) and microstructural effects on strength. In the same study by Charmi et al. [17], they use a crystal plasticity model with RVEs to predict the tensile stress-strain curve. The strength (yield and UTS) was higher in the X direction (581 MPa, 690 MPa) compared to the Z direction (512 MPa, 616 MPa), respectively (see Table 1). The crystal plasticity model was calibrated based on a single tensile test (and EBSD texture measurement) from the 45° sample. The simulations for X and Z samples predicted the stress-strain response within 5% error for

strains between 0.004 and 0.15. At lower strains, there is some disagreement between the simulations and experiments, which may be due to a lack of deformation twinning in the model. It's argued that crystallographic texture is the primary source of the plastic anisotropy. This is justified because grain morphology and porosity (lack of fusion defects) were ruled out as significant factors: the porosity measured from X-ray computed tomography (XCT) was <0.01%, with spherical pores, and the average grain aspect ratio was close to 1 and set to 1 in simulations (the aspect ratio distribution was not reported). It is also notable that the measured reduction in area (analogous to elongation) was similar, not anisotropic, between all three specimens: X, 45°, and Z.

In a more extreme case of plastic anisotropy, Wang et al. [22] built highly textured (single crystal like or oligocrystalline) LPBF 316L with a Goss ((110)<001>) texture (intensity of 21 m.u.d.) on the sample XY plane, and performed tensile tests on specimens that were selectively extracted in the X, Z, and 35° declination from Z for tensile axis alignment along the (100), (101), and (111) crystal directions. A summary of key details and mechanical properties is given in Table 2. The specimens were 99.8% ± 0.1% dense with no indication of lack of fusion porosity from optical micrographs. The three specimens show significant anisotropy in yield, UTS, and elongation. The authors show that the Schmid's law is a good predictor for the strength anisotropy of these oligocrystals: 30% higher strength in (111) direction compared to (100) and (101). However, the (100) and (101) samples are predicted to have the same strength whereas the measured (101) has the lowest strength. This is believed to be due to the elongated grain structure with the (101) Z specimen having a twofold higher grain boundary spacing in the tensile axis direction compared to the (100) X specimen. However, the authors also note there is a significant difference in deformation twinning between the two specimens with prevalent twinning observed at 0.1 strain and predicted to occur near the yield stress for the (101) specimen compared to no twinning in the (100) specimen. The Schmid factor analysis does not consider twinning deformation (only slip on crystallographic planes is considered), so it is also possible that this contributes to the deviation from the predicted strength anisotropy from Schmid's law. The work-hardening (leading to differences in UTS) and elongation anisotropy are discussed considering twinning deformation differences. Very little accreditation is given to microstructure morphology (grain shape or porosity) for the anisotropic UTS and elongation. This study emphasizes the significant role that crystallographic texture, in the extreme case of oligocrystals, has on mechanical anisotropy of strength and UTS for LPBF metals.

Table 2. Anisotropic Young’s yield stress, ultimate tensile strength, and elongation reported by Wang et al. [22] for 316L stainless steel. Values listed are presumed to be the average \pm one standard deviation. The number of measurements for each property is not specified.

		Microstructure			
AM Process	Material	Porosity	Grain Morphology	Crystal Texture	Residual Stress
LPBF	316L Stainless Steel	$< 0.2\% \pm 0.1\%$, spherical	Elongated in Z	Goss: (110) in the Z-axis with an intensity of 12 m.u.d., (100) in X with 21 m.u.d.	n.a.
Tensile Properties					
Sample	Modulus (GPa)	Yield (MPa)	UTS (MPa)	Elongation (%)	Fracture Surface
X (100)	n.a.	546.1 ± 10.0	645.4 ± 1.1	36.2 ± 0.9	n/a
Z (101)	n.a.	495.4 ± 15.1	607.2 ± 11.3	96.3 ± 3.0	n/a
35° (111)	n.a.	710.0 ± 11.6	840.8 ± 10.1	58.5 ± 2.4	n/a

In summary, crystallographic texture is a significant contributor to elastic and plastic anisotropy in AM metals. Elastic and plastic anisotropy can be predicted from elasticity theories and crystal plasticity simulations provided elastic constants, crystallographic texture measurements, and a calibrated crystal plasticity model exist. The extent that crystallographic texture contributes to elastic and plastic anisotropy will greatly depend on the constituent (single crystal) anisotropy, texture components, and the texture intensities. This will depend on the alloy, AM process parameters, and post-processing heat treatments. Crystallographic texture measurements via EBSD, X-ray diffraction (XRD), and neutron diffraction are critical for estimating the role it plays in mechanical anisotropy for a given AM metal.

2.2. Grain and phase morphology

2.2.1. Elongated grains and anisotropic yield strength

Elongated grains in the build direction are common in LPBF metals due to the re-melting and competitive growth process, which allows for easy growth crystals to develop spanning multiple melt tracks and layers. This scenario occurs when the local thermal gradient repeatedly aligns with the preferred crystal growth direction that matches the crystal direction of previous unmelted layers [8]. Figure 2 shows example micrographs of elongated grains in LPBF from two references. This is commonly observed through two-dimensional (2D) cross-sections. Three-dimensional (3D) datasets of grains are rare and

indicate that grain morphology is far more complex than what appears from 2D cross-sections as evidenced by Rowenhorst et al. [23] via serial sectioning and electron backscatter diffraction (EBSD). The elongated grain structure in the build direction is often cited as the culprit for anisotropic mechanical properties based on the idea that there is an effective grain size that is largest in the build direction (Z) and smallest perpendicular to the build direction (X/Y).

First, we will look at the argument for anisotropic strength. The smaller effective grain size for tensile loading in the X/Y direction results in a higher strength due to the phenomenological Hall-Petch effect of increasing strength proportional to one over the square root of the grain size. The literature on this subject shows that this concept is oversimplified, and the effect of grain shape on strength is secondary to the effect of crystallographic texture [24-29]. The simple description of the smallest effective grain size perpendicular to the build direction does not consider the alignment of slip systems within the elongated grains. The interaction between grain shape and different textures (crystals and their slip systems) means that each grain shape and slip plane has an effective grain size based on how the slip plane bisects the elongated grain [30]. Jiang et al. [29] incorporated grain shape into a crystal plasticity model using this concept and demonstrated that for a (100) texture in the same direction as the major axis of elongated grains (aspect ratios of 1, 1.2, and 5), there is no change in anisotropy between an aspect ratio of 1 (equiaxed) and 5. In contrast, a fiber texture results in a slight increase in anisotropy for a grain aspect ratio of 5 compared to equiaxed grains. They hypothesize that because face-centered cubic (FCC) crystals have an abundance of slip systems compared to body-centered cubic (BCC) or HCP crystals, the effect of grain shape is less pronounced, meaning the effective grain size for active slip systems does not change significantly for tensile loading along the major and minor axes of the elongated grains. In addition, Delannay and colleagues [24, 25] have shown that texture and grain morphology have a combined effect on plastic anisotropy. They found better predictions from simulations when accounting for grain shape in addition to texture for tensile tests of electrodeposited iron and rolled steel sheets, which contain strong textures and elongated grain structure. Grain shape, particularly elongated grains, influences anisotropic strength; however, the evidence so far suggests the elongated grain structure is a secondary, non-negligible effect compared to crystallographic texture on anisotropic strength. It would be useful to further study the interaction of grain shape on plastic anisotropy for common AM alloys and textures.

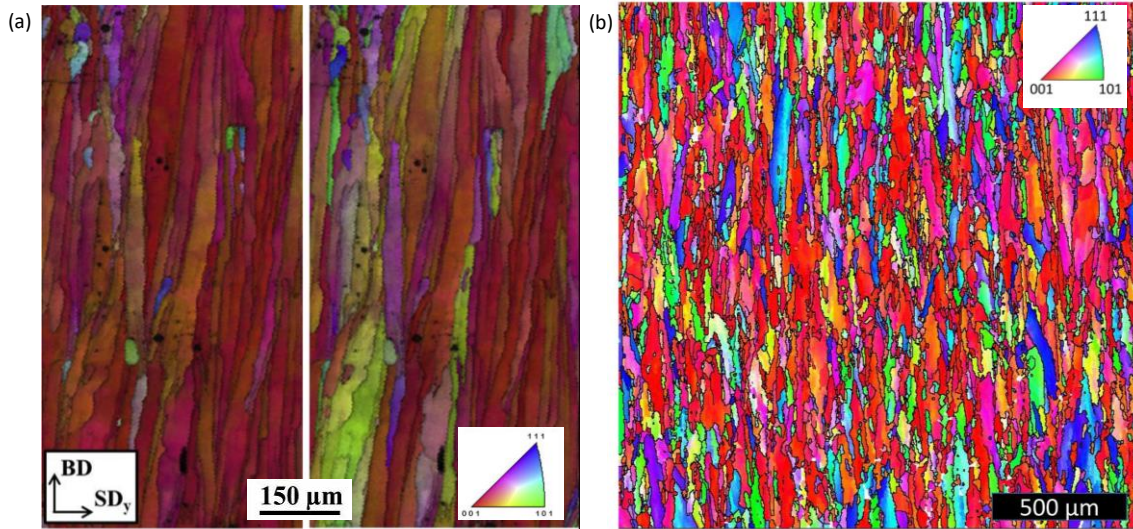


Fig. 2. elongated grains in the build direction for LPBF (a) high silicon steel reused from Ref. [31] under Creative Commons CC-BY license, and (b) nickel superalloy 625 reused from Ref. [32] with permission.

2.2.2. Microstructure morphology and anisotropic elongation

Anisotropic microstructure morphologies lead to anisotropic elongation. These include elongated grains, grain boundary textures (different but related to crystallographic texture), and preferential distributions of secondary phases or features. Glaring examples exist for secondary phases/features in AM Ti-6Al-4V and conventionally processed alloys, while grain boundary textures have been less studied. In all cases, the elongated grain structure cannot be separated from these other sources of anisotropic elongation. Here we argue that these other sources associated with elongated grains are the causes that require more focus rather than attribution to the elongated grain structure itself. Porosity is discussed separate of this section, and the examples reviewed have very low porosity and no evidence of lack of fusion porosity defects.

A commonly studied feature in AM Ti alloys is the grain boundary alpha-phase [33]. Grain boundary alpha occurs in conventionally processed and AM Ti alloys, is morphologically different than the alpha that forms within grains or colonies and is known to reduce fracture toughness [34, 35]. Examples of grain boundary alpha are shown in Fig. 3. In AM Ti-6Al-4V, anisotropic elongation has been observed in EPBF, DED, and LPBF Ti-6Al-4V and linked to grain boundary alpha [36-38]. The grain boundary alpha forms at the prior beta grain boundaries, which are elongated in the build direction. Prior beta refers to the beta grain structure that forms prior to the phase transformation from beta to alpha upon cooling. The elongated prior beta grain microstructures can be determined from EBSD data and the alpha-beta crystal orientation relationship [39]. Microstructurally, this results in elongated grain boundary alpha in the build direction. Mechanically, this results in lower elongation to failure in the X/Y direction compared to the Z direction. The grain boundary alpha is believed to act as damage initiation sites, making the material easier to fracture, reducing elongation when

the grain boundary alpha is loaded perpendicularly (loading in the X/Y direction). This cause for anisotropic elongation has been isolated from crystallographic texture and porosity. For example Carroll et al. [37] have noted that AM Ti-6Al-4V has only a weak alpha-phase texture even though a strong prior beta grain texture exists due to twelve crystallographic alpha variants that form from beta phase. In addition, they report yield strength and UTS are nearly identical in both X/Y and Z directions for DED Ti-6Al-4V [37], which could not occur if a strong alpha texture exists because single crystal alpha phase is highly plastically anisotropic. Lastly, a very low porosity 0.001% with only spherical pores was measured with XCT in this study ruling out its role in anisotropic elongation [37]. Wilson-Heid et al. [38] observed the same thing for LPBF Ti-6Al-4V: very little anisotropic yield strength and significant anisotropic elongation, in addition to an increase in anisotropic elongation with an increase in prior beta grain aspect ratio, summarized in Table 3. The increase in prior beta grain boundary aspect ratio would increase the length of grain boundary alpha, creating longer paths for cracks to form and travel, which supports the hypothesis that elongated grain boundary alpha in the build direction is the cause for anisotropic elongation in these studies.

Table 3. Anisotropic tensile elongation reported by Wilson-Heid et al. [38] for Ti-6Al-4V. Note two different sized tensile specimens were used for pulsed laser (P) and continuous wave laser (CW) samples. Values listed are the average \pm one standard deviation. The number of measurements for mechanical properties ranges from 3 to 16.

Microstructure					
AM Process	Material	Porosity	Grain Morphology	Crystal Texture	Residual Stress
LPBF: Pulsed laser (P) and continuous wave (CW)	Ti-6Al-4V	99.7% \pm 1.3%, 98.7% \pm 2.2%, 98.2% \pm 1.9%, spherical pores	Alpha laths, nearly equiaxed (1.2 aspect ratio) prior beta (CW) to elongated (8.0 aspect ratio) prior beta (P)	n.a.	n.a.
Tensile Properties					
Sample	Modulus (GPa)	Yield (MPa)	UTS (MPa)	Elongation (%)	Fracture Surface
CW X	103 \pm 2.0	1137 \pm 10.3	1204 \pm 13.0	8.5 \pm 1.1	n.a.
CW Z	103 \pm 2.4	1141 \pm 1.5	1207 \pm 6.7	12.7 \pm 1.1	n.a.
P X	110 \pm 5.6	1078 \pm 2.9	1131 \pm 17.4	2.8 \pm 0.8	n.a.
P Z	110 \pm 4.6	1010 \pm 0.0	1117 \pm 1.2	7.8 \pm 1.1	n.a.

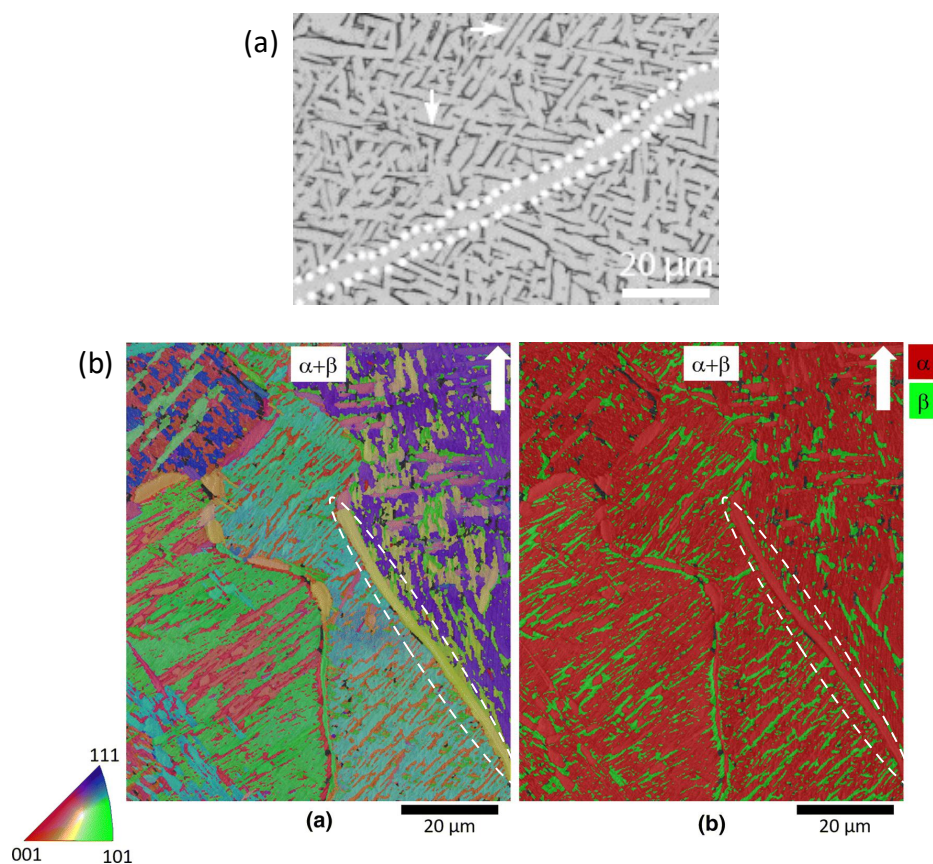


Fig. 3. Examples of grain boundary alpha highlighted with dotted outlines in (a) Ti-6Al-4V reused from Ref. [40] under Creative Commons Attribution 3.0 license, and (b) post-processed LPBF Ti-6Al-4V-3Fe alloy reused from Ref. [41] under Creative Commons Attribution 4.0 International license.

The preferential location/direction of precipitates is also a significant cause for anisotropic elongation and fracture. This is widely true for conventionally processed alloys. For example, Ghosh et al. [42] report stringer type (collection of inclusions distributed along a preferred direction) MnS inclusions in low-carbon ferritic steel cause anisotropic fracture toughness and tensile ductility. An example in AM metals has been reported for wire-arc AM (WAAM) Ti-6Al-4V with trace amounts of LaB₆ and B. These elements were introduced to refine the microstructure, reduce dissolved oxygen, and improve mechanical properties [43]. While the strength increased after adding LaB₆ and B, the anisotropy in elongation also increased with an overall decrease in elongation. LaB₆ and B free Ti-6Al-4V showed anisotropic elongation to fracture with 24% and 20% in the Z and X directions, respectively for reasons previously discussed, while doped Ti-6Al-4V showed 14% to 18% and 5% to 8% in the Z and X directions, respectively, due to highly aligned needlelike precipitates along the build direction. These highly aligned, coarse precipitates create an easy path for crack initiation and propagation when the sample is loaded in the X direction, which results in overall lower and more anisotropic elongation compared to the already anisotropic WAAM Ti-6Al-4V.

A less emphasized source of anisotropic elongation is the combination of elongated grains and their grain boundary character. Describing the grain boundary character requires the misorientation between the two crystals that make the boundary and the orientation of the grain boundary plane normal (five terms in total) [44]. A few common categorization methods are high and low angle boundaries based simply on misorientation, coincident site lattice theory that identifies grain boundaries with a more regular structure than general boundaries, and grain boundary energy [45]. The preferential existence of specific grain boundaries is akin to crystallographic texture and referred to as grain boundary texture [46]. It is not always clear what constitutes a special grain boundary or which boundaries may be beneficial or detrimental [47]. However, in some instances the early onset of cracking is linked to specific boundary types and ductility may be improved through grain boundary engineering [48, 49]. The sensitivity to grain boundary types is more prevalent when fracture occurs along grain boundaries rather than trans-granularly. Connectivity of grain boundary types is also an important factor [49, 50], particularly for AM microstructures for which the elongated grains can lead to more connectivity or longer paths for cracks to propagate in the build direction. More recent studies have focused on grain boundary character for AM metals to apply grain boundary engineering concepts for improved mechanical performance in corrosive environments [51-54]. The roles that grain boundary character and morphology play on room temperature tensile anisotropy of LPBF metals has not been extensively studied. However, based on the literature this should be studied further as a possible source of anisotropic elongation.

In summary, the broad statement that anisotropic microstructures lead to anisotropic elongation is true, but the specifics require more details. Highly aligned microstructure features that act as damage initiation sites and provide long crack paths, such as grain boundary alpha and precipitates, will cause reduced elongation when loaded perpendicularly to the preferential direction, which results in anisotropic elongation. These features may be the result of the elongated grain structure that forms; however, anisotropic tensile properties are not necessarily due to elongated grains directly. The role of grain shape and grain boundary character on anisotropic elongation should be studied further through EBSD, grain boundary analyses, and in-situ or interrupted tensile testing to observe deformation evolution at the microstructural level.

2.3. Lack of fusion defects and anisotropic elongation

Defects, namely porosity, exist in additive manufacturing. Lack of fusion defects are characterized by irregular shapes or sharp edges that occur when insufficient melting occurs. An example of lack of fusion defects is shown in Fig. 4. Insufficient melting between laser tracks often results in elongated porosity defects along the laser track. This can occur because of an irregularity at a single point or occur systemically because of a lack of optimized, robust process parameters. Lack of fusion pores that occur systemically create defects that follow the laser scanning (layer-by-layer) structure. The irregular defects act as stress-concentrators and combined with their alignment along a layer make it easy for cracks to propagate parallel to the layer structure. This results in lower elongation for loading in the build (Z) direction compared to X and Y. Note that

this is the opposite elongation trend for the case of grain boundary alpha in Ti-6Al-4V. Isolating the effects of lack of fusion defects can be achieved by post-processing heat-treatments that eliminate other contributing factors to anisotropic elongation.

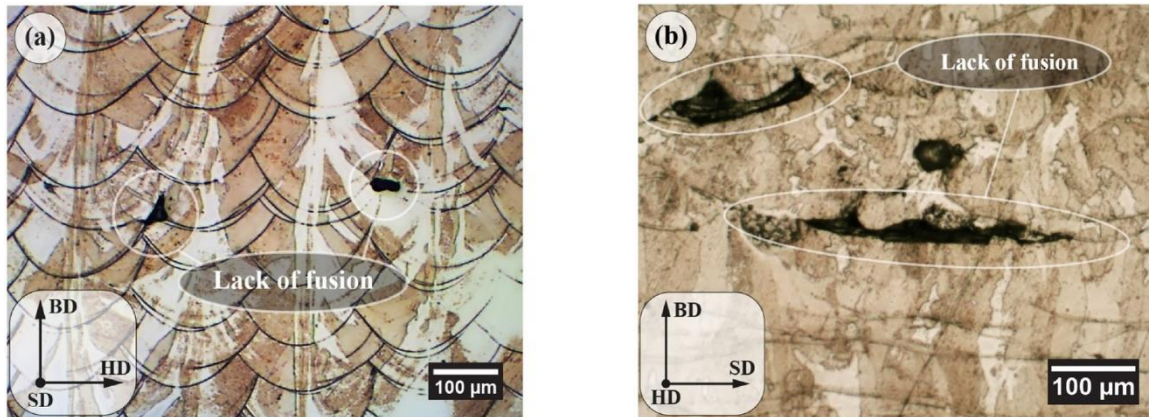


Fig. 4. Lack of fusion defects circled for emphasis for a cross-section of the (a) scan direction (SD) and (b) hatch direction (HD) reused from [55] under Creative Commons CC-BY license. The combination reveals the elongated nature of lack of fusion defects along the scanning direction.

One exemplar study by Ronneberg et al. [55] provides strong evidence that lack of fusion defects are not a source of anisotropic yield strength and are a significant source of anisotropic elongation. They characterized LPBF 316L stainless steel that contained lack of fusion defects (~99.5% dense and pore aspect ratio of 2.4 to 3.1). The elongation to failure was smaller for vertical (Z) samples compared to horizontal samples (X) samples in the as-built (machined surface) condition. In addition, the yield strength was lower for vertical (Z) samples compared to horizontal samples (X). After homogenization and annealing heat-treatments (removes chemical segregation and causes grain growth), the anisotropic elongation remained (although the total elongation increased) and the anisotropic yield strength was eliminated. The heat treatments have no effect on the lack of fusion defects. Ronneberg et al. [55] conclude that since the yield strength anisotropy was eliminated while the lack of fusion defects remain, the anisotropic yield strength was caused by something other than porosity. They further argue that the anisotropy in elongation was primarily due to lack of fusion defects because the anisotropy in elongation remained after heat treatments wiped out chemical segregation, melt pool boundaries, and heterogeneous dislocations. The tensile properties are summarized in Table 4. The study lacks quantitative characterization of crystallographic texture and grain morphology; however, it still provides strong evidence that lack of fusion porosity is linked to anisotropic elongation and not linked to anisotropic yield stress.

Table 4. Anisotropic tensile elongation reported by Ronneberg et al. [55]. Yield stress values are the range of reported values. Elongation is the linear best fit value. Elongation measurements showed significant scatter. The reader is referred to the original reference for more details.

		Microstructure			
AM Process	Material	Porosity	Grain Morphology	Crystal Texture	Residual Stress
LPBF	316L Stainless Steel	0.26% to 0.66% Aspect Ratio 2.4 to 3.1	n.a.	n.a.	n.a.
Tensile Properties					
Sample	Modulus (GPa)	Yield (MPa)	UTS (MPa)	Elongation (%)	Fracture Surface
As-built X	n.a.	500 to 515	n.a.	23.7	connected multiple lack of fusion pores without a straight profile between them
As-built Z	n.a.	414 to 447	n.a.	2.3	coalescence of lack of fusion pores by crack growth along the layer boundaries
Homogenized 900 °C X	n.a.	368 to 395	n.a.	28.2	surfaces are less orthogonal to the loading direction but with evidence of porosity coalescence leading to failure
Homogenized 900 °C Z	n.a.	362 to 377	n.a.	9.7	
Annealed 1200 °C X	n.a.	255 to 274	n.a.	29.74	
Annealed 1200 °C Z	n.a.	270 to 277	n.a.	12.2	

Prasad et al. [56] simulated the effect of porosity and pore shape on the stress-strain response of 316L stainless steel using a crystal plasticity model with damage evolution for the growth and coalescence of the pores. The authors used RVEs with a fixed grain size, grain shape elongated in the build direction (Z), and a nearly uniform crystal orientation distribution (no texture) while changing the porosity from 0%, 2%, and 8% and the pores shape from equiaxed to elongated in the build direction with an aspect ratio of 3. Note that this porosity (2% and 8%) and the morphology (major axis along the build direction) while possible in LPBF is not necessarily a realistic representative of lack of fusion defects, which is more commonly < 1% and oriented with the major axis perpendicular to the build direction (e.g., [55]). However, it provides some insight into the role of elongated pores on mechanical behavior. Prasad et al. [56] find that increasing porosity leads to decreasing strength observed in the form of lower flow stress for equivalent stress-equivalent plastic strain curves. Second, they find that elongated pores

introduce anisotropy in the onset of plastic instability (akin to the ultimate tensile stress and strain). The instability strain in the uniaxial tension simulation occurs when significant damage via coalescence of pores occurs leading to unstable deformation, a precursor to complete failure. For an RVE with spherical pores and 8% porosity the instability stress and strain are approximately equal along the build (Z) direction and transverse (X/Y) direction. The ratio of the build direction to transverse direction instability stress and strain were 1.00 and 1.04, respectively. It's safe to assume that this nearly isotropic response holds true for 2% equiaxed pores too. For elongated pores with the major axis parallel to the build direction the instability stress and strain ratios increase to 1.05 and 1.43 for 2% porosity and 1.11 and 2.00 for 8% porosity, respectively. The elongated pores create anisotropy in the instability strain. The instability strain is significantly smaller when the loading axis is perpendicular to the major axis of the elongated pores. These simulations support the findings that elongated pores create anisotropy in elongation to failure with lower elongation values when the major pore axis is loaded perpendicularly.

2.4. Melt pool structure and anisotropic elongation

The LPBF process subjects material to multiple cycles of melting and solidification, which exhibit distinct microstructure and macrostructure variation. In conventional materials processing, macrostructure is used to differentiate the aspects of the material structure that exist at a coarser scale than other microstructure features such as in large weldments and billets with location specific microstructures. In additive manufacturing, macrostructure is primarily used to describe the structure associated with the melt-pools (many small weldments), which is one of the larger components of internal structure but not necessarily the largest (e.g., existence of continuous grains through melt-pools). The melt pool macrostructure is comprised of overlapping individual laser scans that can be seen in etched microstructures as shown in Fig. 5. The melt pool macrostructure can be broken into three distinct microstructure morphologies or regions as shown in Fig. 6. These are areas with a coarser and more varied microstructure (1), areas with a finer and more equiaxed microstructure (3) and a sort of a heat affected transition zone (HAZ) in between the two previously mentioned ones (2). While the extent of this differentiation is dependent on the alloy (Fig. 5 and Fig. 6 are for AlSi10Mg), this type of macrostructure and the directionality occurs for most LPBF alloys. This can be seen for Ti6Al4V in [57] and for SS316 in [58].

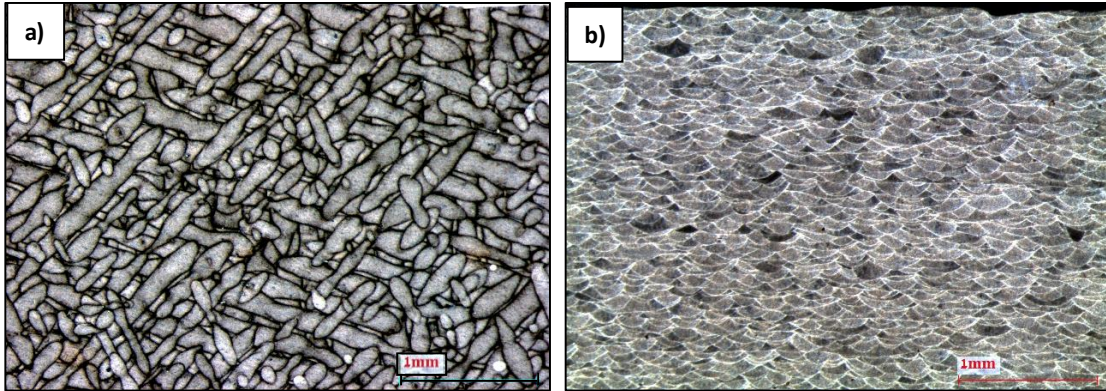


Fig. 5. Macrostructure of the SLM AlSi10Mg Alloy: a) Top view revealing the track segment morphology and the 67° rotation of the laser relating to the scan strategy; b) Side view revealing the “fish scale” morphology and the overlapping melt pools. Figures reused from Ref. [59] with permission.

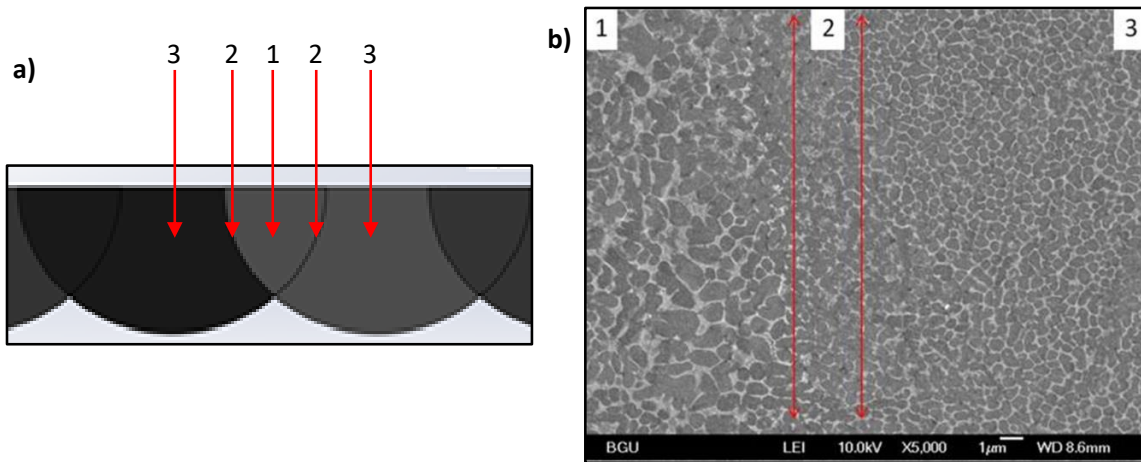


Fig. 6. Microstructure morphologies for an AlSi10Mg alloy: a) Melt pool schematic showing the zone locations b) matching microstructure zones: 1 – Coarse fusion zone, 2- Transition zone (referred to as HAZ), 3 – Fine fusion zone. Figures reused from Ref. [59] with permission.

The contribution of the part macrostructure to the mechanical properties and elongation anisotropy is not a common focus in conventional mechanical analysis. Melt pool boundaries may create microstructures and/or defects that create localized deformation at layer-to-layer boundaries. This means that elongation to failure will be lower in the Z direction (layer-to-layer boundaries are loaded perpendicularly) compared to the X direction for a typical rotating scan strategy. It also means that Z direction fracture surfaces will follow the layer and/or melt pool structure. In many of the aforementioned studies, samples were characterized in the as-built or stress-relieved condition, which contain their melt pool structure; however, the mechanical anisotropy was sufficiently explained by other sources. Thus, the macrostructure is not always a significant source of mechanical anisotropy. It may be a source of anisotropic elongation when precipitate, grain structure, or defect heterogeneity follow melt pool boundaries. It’s not always clear when and why

the melt pool boundary is a significant source of anisotropy. Fracture surface morphology is the best indicator to implicate melt pool boundaries as a source of anisotropic elongation to fracture [58-61].

Anisotropic elongation between the vertical (Z) and horizontally built (X/Y) parts has been observed in a variety of investigations of AlSi10Mg [60, 61]. Rosenthal et al. [60] show there is no difference in yield stress values between orientations but a prominent difference in elongation is apparent with higher elongation for X specimens compared to Z specimens (see Table 5). There is no quantitative porosity, grain size, or texture analysis. However, Rosenthal et al. [60] show convincing evidence that fracture occurs along melt pool track boundaries following the layer structure for Z samples compared to more undulating fracture paths for X samples, as shown in Fig. 7. Rosenthal et al. [60] report partial track segments equivalent in magnitude to the hatching distance on the Z specimen and that one side of the fracture surface displayed “empty” traces of the segments while the other side contained the remainder of the separated track. For the AlSi10Mg alloy, the coarser fusion zone (Fig. 6, Zone 1) and boundary between the coarse and fine fusion zones (Fig. 6, Zone 2) are arguably weaker locations compared to the fine fusion zone microstructure (Fig. 6, Zone 3) due to reductions in Hall-Petch, second phase, and coherency strengthening. The weaker zones could allow for easier crack propagation serving as the origin of failure.

Table 5. Anisotropic tensile elongation for LPBF AlSi10Mg reported by Rosenthal et al. [60]. Values are the average \pm one standard deviation from 5 measurements.

		Microstructure			
AM Process	Material	Porosity	Grain Morphology	Crystal Texture	Residual Stress
LPBF Ref [60]	AlSi10Mg	n.a.	n.a.	n.a.	Stress-relieved 2 hours at 300 °C
Tensile Properties					
Sample	Modulus (GPa)	Yield (MPa)	UTS (MPa)	Elongation (%)	Fracture Surface
X	n.a.	182 \pm 5	282 \pm 5	25.2 \pm 1.0	Undulating
Z	n.a.	184 \pm 5	288 \pm 5	18.3 \pm 1.0	Planar with partial track segments

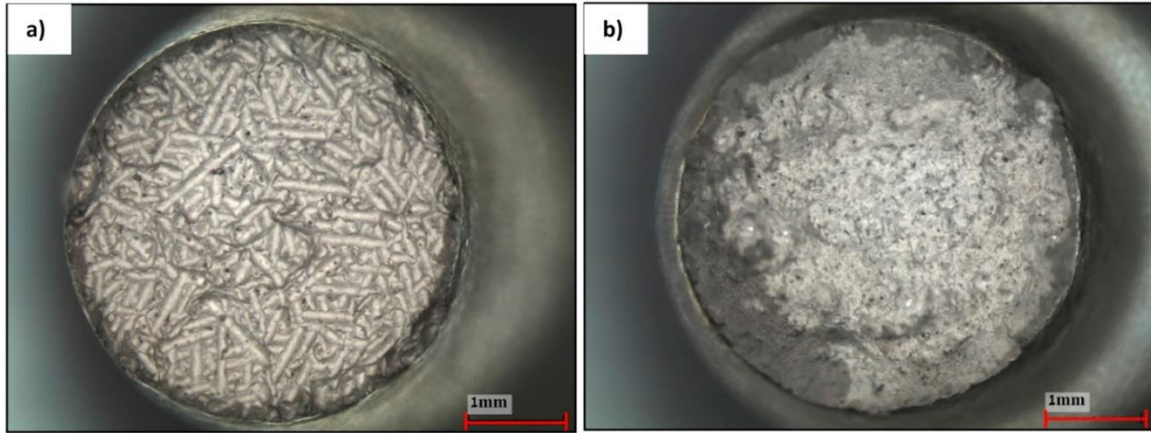


Fig. 7. AlSi10Mg fracture surfaces for (a) loading along Z-axis and (b) loading along X-axis reused from Ref. [60] with permission.

Shifeng et al. [58] document and discuss the role of melt pool structure on anisotropic elongation and fracture surfaces for LPBF 316L stainless steel. They used a raster scan strategy in the Y direction as opposed to rotating the scan direction between layers and tested samples at different angles in the X-Y plane (all horizontal specimens with different angles with respect to the scanning direction) and different inclination angles with respect to the Z-axis (ranging from horizontal to completely vertical). Shifeng et al. [58] acknowledge the likelihood of a (100) texture along the build direction (Z); however, characterization of porosity, crystal texture, and grain morphology are absent. Therefore, a complete summary of the trends in their work are not reported here. Rather, only the strongest evidence from their work that melt pool structure influences tensile properties is reviewed. Shifeng et al. [58] categorize melt pool boundaries into layer-layer and track-track boundaries where the later are the boundaries between adjacent tracks in the same layer. Among the horizontal specimens (X/Y) at different angles with respect to the scanning direction, they observe lower yield strength and elongation (average \pm one standard deviation from three measurements) when the loading axis is perpendicular to the laser scanning direction (perpendicular to track-track boundaries): $624 \text{ MPa} \pm 73 \text{ MPa}$ and $15.6\% \pm 5.1\%$. Vertical (Z) specimens show higher ductility than all horizontal specimens ($632 \text{ MPa} \pm 10 \text{ MPa}$ and $49.7\% \pm 0.7\%$), which is the opposite of the trend reported for AlSi10Mg with lower ductility for vertical (Z) specimens compared to horizontal (X/Y) specimens. Accompanying these trends are observations that fracture surfaces tend to follow track-track and layer-layer melt pool boundaries. Schematics from Shifeng et al. [58] and Rosenthal et al. [60] are given in Fig. 8. There is a significant difference in horizontal specimen fracture surfaces due to scan strategy differences (uni-directional raster vs. rotated); whereas the fracture surfaces in the vertical direction follow melt pool boundaries regardless. It is difficult to completely isolate the melt pool microstructure from crystal texture and lack of fusion. Macrostructure analysis should be employed with other alloys to account for all possible sources of anisotropic elongation. Characterizing fracture surfaces is particularly useful for this purpose.

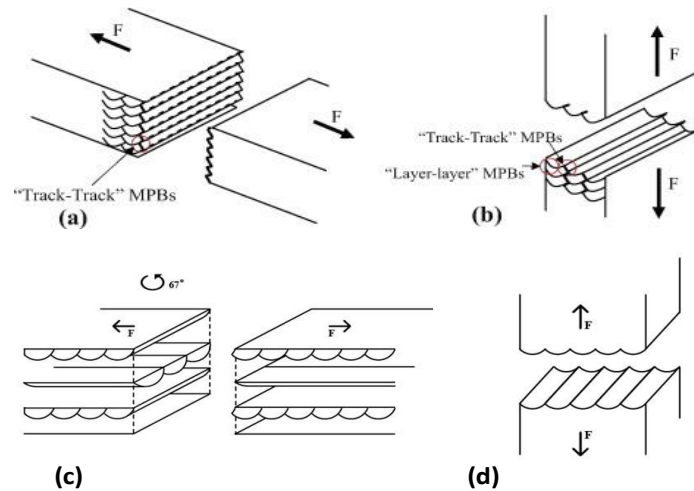


Fig. 8. Melt pool boundary (MPB) structure and fracture surface schematics for (a) horizontal (X) and (b) vertical (Z) specimens for a uni-directional raster scan strategy in the Y-direction reused from Ref. [58] with permission, (c) horizontal (X/Y) and (b) vertical (Z) specimens for a rotating (67°) scan strategy reused from Ref. [60] with permission.

2.5. Residual Stresses

Residual stresses are inherent to the AM process [62, 63]. Residual stresses are related to the localized melting and rapid solidification. The hotter solidifying deposited layer wants to contract while the cooler base material does not. This creates a tensile residual stress in the deposited layer and compressive residual stress in the base material. The development of residual stresses in LPBF metals is more complicated than this simple description due to the remelting of layers, anisotropy in residual stress along the laser scan direction, and varying scan strategies employed [62, 63]. High residual stresses can lead to processing or final geometry errors caused by part deflection. Residual stresses can be removed through application of heat treatments and mitigated through build plate or powder bed heating and modifications to laser scan strategies [63]. Bartlett and Li [62] note that anisotropic static mechanical properties are often related to the factors discussed in previous sections; however, residual stress has been linked to lower fatigue and fracture properties as well as anisotropic fatigue and fracture properties. The combination of tensile residual stresses and porosity defects LPBF metals is particularly potent for reducing fatigue life [62]. Anisotropic dynamic mechanical properties are outside the scope of this review.

3. Summary

This review has provided detailed examples of the sources of tensile property anisotropy for LPBF alloys, which are primarily crystallographic texture, anisotropic microstructure morphologies, lack of fusion defects, and macrostructure (melt pools). Within anisotropic microstructures, elongated grains appear to be secondary compared to the preferential distribution of phases and features (e.g., grain boundary alpha, precipitates, etc.). The

findings for one set of laser process parameters and alloy are not prescriptive. It's essential that the sources listed above should be characterized before associating the cause of tensile anisotropy to a particular source. **Table 6** provides a succinct summary of each source of anisotropy, the primary and secondary tensile properties affected, and experimental measurements for quantitative microstructure analysis. There are challenges assessing the cause of tensile anisotropy. Quantitative microstructure analysis may require 3D measurements and micrographs from multiple planes at a minimum. Some sources such as the melt pool macrostructure are difficult to isolate. Furthermore, interactions between sources may amplify anisotropy. Physics based models are critical for turning on or off certain sources of anisotropy to study their behavior. A clearer understanding of the importance of each source of anisotropy for a particular alloy and additive process is necessary to predict and control tensile anisotropy in metals-based LPBF.

Table 6. Summary of tensile anisotropy sources, properties, and micro/macro-structure measurements for LPBF alloys. EBSD – electron backscatter diffraction. EDS – energy dispersive x-ray spectroscopy

Anisotropy source	Primary Tensile Property Anisotropy	Secondary Tensile Property Anisotropy	Micro/macro structure characterization
Crystal texture	Modulus, yield stress	Ultimate tensile strength, elongation	EBSD, X-ray diffraction
Elongated grains		Yield stress	Optical and electron micrographs including EBSD
Preferential phases/features	Elongation		Optical and electron micrographs; EDS and EBSD
Lack of fusion defects	Elongation		Optical micrographs, X-ray microtomography
Melt pools	Elongation		Optical and electron micrographs

References

- [1] ASTM (2014)– *F3122-14 Standard Guide for Evaluating Mechanical Properties of Metal Materials Made via Additive Manufacturing Processes* (ASTM International, West Conshohocken, PA). <https://doi.org/10.1520/F3122-14>
- [2] ISO / ASTM (2019)– *52921-13 Standard Terminology for Additive Manufacturing-Coordinate Systems and Test Methodologies* (ASTM International, West Conshohocken, PA). <https://doi.org/10.1520/ISOASTM52921-13R19>

- [3] ASTM (2014)– *F3055-14a Standard Specification for Additive Manufacturing Nickel Alloy (UNS N07718) with Powder Bed Fusion* (ASTM International, West Conshohocken, PA). <https://doi.org/10.1520/F3055-14A>
- [4] America Makes and ANSI Additive Manufacturing Standardization Collaborative (2018) *Standardization Roadmap for Additive Manufacturing. Version 2.0.* June 2018.
- [5] ASTM (2015)– *WK49229 New Guide for Orientation and Location Dependence Mechanical Properties for Metal Additive Manufacturing* (ASTM International).
- [6] Lewandowski JJ , Seifi M (2016) Metal Additive Manufacturing: A Review of Mechanical Properties. *Annu Rev Mater Res* 46:14.11-14.36.
- [7] Kok Y, Tan XP, Wang P, Nai MLS, Loh NH, Liu E, Tor SB (2018) Anisotropy and heterogeneity of microstructure and mechanical properties in metal additive manufacturing: A critical review. *Materials & Design* 139:565-586. <https://doi.org/10.1016/j.matdes.2017.11.021>
- [8] DebRoy T, Wei HL, Zuback JS, Mukherjee T, Elmer JW, Milewski JO, Beese AM, Wilson-Heid A, De A, Zhang W (2018) Additive manufacturing of metallic components – Process, structure and properties. *Progress in Materials Science* 92:112-224. <https://doi.org/10.1016/j.pmatsci.2017.10.001>
- [9] Bunge HJ (1982) *Texture Analysis in Materials Science* (Butterworths).
- [10] Kocks UF, Tomé CN, Wenk H-R (2000) *Texture and anisotropy: preferred orientations in polycrystals and their effect on materials properties* (Cambridge university press).
- [11] Sofinowski KA, Raman S, Wang X, Gaskey B, Seita M (2021) Layer-wise engineering of grain orientation (LEGO) in laser powder bed fusion of stainless steel 316L. *Additive Manufacturing* 38:101809. <https://doi.org/10.1016/j.addma.2020.101809>
- [12] Gokcekaya O, Hayashi N, Ishimoto T, Ueda K, Narushima T, Nakano T (2020) Crystallographic orientation control of pure chromium via laser powder bed fusion and improved high temperature oxidation resistance. *Additive Manufacturing* 36:101624. <https://doi.org/10.1016/j.addma.2020.101624>
- [13] Wang Y , Shi J (2020) Developing very strong texture in a nickel-based superalloy by selective laser melting with an ultra-high power and flat-top laser beam. *Materials Characterization* 165:110372. <https://doi.org/10.1016/j.matchar.2020.110372>
- [14] Hill R (1952) The Elastic Behaviour of a Crystalline Aggregate. *Proceedings of the Physical Society Section A* 65(5):349.
- [15] Man C-S , Huang M (2011) A Simple Explicit Formula for the Voigt-Reuss-Hill Average of Elastic Polycrystals with Arbitrary Crystal and Texture Symmetries. *Journal of Elasticity* 105(1):29-48. <https://doi.org/10.1007/s10659-011-9312-y>
- [16] Mainprice D, Hielscher R, Schaeben H (2011) Calculating anisotropic physical properties from texture data using the MTEX open-source package. *Geological Society, London, Special Publications* 360(1):175-192. <https://doi.org/10.1144/sp360.10>
- [17] Charmi A, Falkenberg R, Ávila L, Mohr G, Sommer K, Ulbricht A, Sprengel M, Saliwan Neumann R, Skrotzki B, Evans A (2021) Mechanical anisotropy of additively manufactured stainless steel 316L: An experimental and numerical

- study. *Materials Science and Engineering: A* 799:140154.
<https://doi.org/10.1016/j.msea.2020.140154>
- [18] Sun S-H, Hagihara K, Nakano T (2018) Effect of scanning strategy on texture formation in Ni-25at.%Mo alloys fabricated by selective laser melting. *Materials & Design* 140:307-316. <https://doi.org/10.1016/j.matdes.2017.11.060>
- [19] Marattukalam JJ, Karlsson D, Pacheco V, Beran P, Wiklund U, Jansson U, Hjörvarsson B, Sahlberg M (2020) The effect of laser scanning strategies on texture, mechanical properties, and site-specific grain orientation in selective laser melted 316L SS. *Materials & Design* 193:108852.
<https://doi.org/10.1016/j.matdes.2020.108852>
- [20] Choo H, Sham K-L, Bohling J, Ngo A, Xiao X, Ren Y, Depond PJ, Matthews MJ, Garlea E (2019) Effect of laser power on defect, texture, and microstructure of a laser powder bed fusion processed 316L stainless steel. *Materials & Design* 164:107534. <https://doi.org/10.1016/j.matdes.2018.12.006>
- [21] Kunze K, Etter T, Grässlin J, Shklover V (2015) Texture, anisotropy in microstructure and mechanical properties of IN738LC alloy processed by selective laser melting (SLM). *Materials Science and Engineering: A* 620:213-222. <https://doi.org/10.1016/j.msea.2014.10.003>
- [22] Wang X, Muñoz-Lerma JA, Attarian Shandiz M, Sanchez-Mata O, Brochu M (2019) Crystallographic-orientation-dependent tensile behaviours of stainless steel 316L fabricated by laser powder bed fusion. *Materials Science and Engineering: A* 766:138395. <https://doi.org/10.1016/j.msea.2019.138395>
- [23] Rowenhorst DJ, Nguyen L, Murphy-Leonard AD, Fonda RW (2020) Characterization of Microstructure in Additively Manufactured 316L using Automated Serial Sectioning. *Current Opinion in Solid State and Materials Science* 24(3):100819. <https://doi.org/10.1016/j.cossms.2020.100819>
- [24] Delannay L, Melchior MA, Signorelli JW, Remacle JF, Kuwabara T (2009) Influence of grain shape on the planar anisotropy of rolled steel sheets – evaluation of three models. *Computational Materials Science* 45(3):739-743. <https://doi.org/10.1016/j.commatsci.2008.06.013>
- [25] Delannay L, Barnett MR (2012) Modelling the combined effect of grain size and grain shape on plastic anisotropy of metals. *Int J Plasticity* 32-33:70-84. <https://doi.org/10.1016/j.ijplas.2011.12.002>
- [26] Murty KL, Tanikella BV, Earthman JC (1994) Effect of grain shape and texture on equi-biaxial creep of stress relieved and recrystallized zircaloy-4. *Acta Metallurgica et Materialia* 42(11):3653-3661. [https://doi.org/10.1016/0956-7151\(94\)90431-6](https://doi.org/10.1016/0956-7151(94)90431-6)
- [27] Xie Q, Eyckens P, Vegter H, Moerman J, Van Bael A, Van Houtte P (2013) Polycrystal plasticity models based on crystallographic and morphologic texture: Evaluation of predictions of plastic anisotropy and deformation texture. *Materials Science and Engineering: A* 581:66-72.
<https://doi.org/10.1016/j.msea.2013.06.008>
- [28] Mathur KK, Dawson PR, Kocks UF (1990) On modeling anisotropy in deformation processes involving textured polycrystals with distorted grain shape. *Mechanics of Materials* 10(3):183-202. [https://doi.org/10.1016/0167-6636\(90\)90042-E](https://doi.org/10.1016/0167-6636(90)90042-E)

- [29] Jiang M, Devincere B, Monnet G (2019) Effects of the grain size and shape on the flow stress: A dislocation dynamics study. *Int J Plasticity* 113:111-124. <https://doi.org/10.1016/j.ijplas.2018.09.008>
- [30] Bunge H, Wagner F, Van Houtte P (1985) A new way to include the grain shape in texture simulations with the Taylor model. *Journal de Physique Lettres* 46(23):1109-1113.
- [31] Garibaldi M, Ashcroft I, Simonelli M, Hague R (2016) Metallurgy of high-silicon steel parts produced using Selective Laser Melting. *Acta Materialia* 110:207-216. <https://doi.org/10.1016/j.actamat.2016.03.037>
- [32] Zhang F, Levine LE, Allen AJ, Stoudt MR, Lindwall G, Lass EA, Williams ME, Idell Y, Campbell CE (2018) Effect of heat treatment on the microstructural evolution of a nickel-based superalloy additive-manufactured by laser powder bed fusion. *Acta Materialia* 152:200-214. <https://doi.org/10.1016/j.actamat.2018.03.017>
- [33] Tiley J, Searles T, Lee E, Kar S, Banerjee R, Russ JC, Fraser HL (2004) Quantification of microstructural features in α/β titanium alloys. *Materials Science and Engineering: A* 372(1):191-198. <https://doi.org/10.1016/j.msea.2003.12.008>
- [34] Ahmed T, Rack HJ (1998) Phase transformations during cooling in $\alpha+\beta$ titanium alloys. *Materials Science and Engineering: A* 243(1):206-211. [https://doi.org/10.1016/S0921-5093\(97\)00802-2](https://doi.org/10.1016/S0921-5093(97)00802-2)
- [35] Foltz JW, Welk B, Collins PC, Fraser HL, Williams JC (2011) Formation of Grain Boundary α in β Ti Alloys: Its Role in Deformation and Fracture Behavior of These Alloys. *Metall and Mat Trans A* 42(3):645-650. <https://doi.org/10.1007/s11661-010-0322-3>
- [36] Hrabe N, Quinn T (2013) Effects of processing on microstructure and mechanical properties of a titanium alloy (Ti-6Al-4V) fabricated using electron beam melting (EBM), Part 2: Energy input, orientation, and location. *Materials Science and Engineering: A* 573:271-277. <https://doi.org/10.1016/j.msea.2013.02.065>
- [37] Carroll BE, Palmer TA, Beese AM (2015) Anisotropic tensile behavior of Ti-6Al-4V components fabricated with directed energy deposition additive manufacturing. *Acta Materialia* 87:309-320. <https://doi.org/10.1016/j.actamat.2014.12.054>
- [38] Wilson-Heid AE, Wang Z, McCornac B, Beese AM (2017) Quantitative relationship between anisotropic strain to failure and grain morphology in additively manufactured Ti-6Al-4V. *Materials Science and Engineering: A* 706:287-294. <https://doi.org/10.1016/j.msea.2017.09.017>
- [39] Glavicic MG, Kobryn PA, Bieler TR, Semiatin SL (2003) A method to determine the orientation of the high-temperature beta phase from measured EBSD data for the low-temperature alpha phase in Ti-6Al-4V. *Materials Science and Engineering: A* 346(1):50-59. [https://doi.org/10.1016/S0921-5093\(02\)00535-X](https://doi.org/10.1016/S0921-5093(02)00535-X)
- [40] Neikter M, Åkerfeldt P, Pederson R, Antti ML (2017) Microstructure characterisation of Ti-6Al-4V from different additive manufacturing processes. *IOP Conference Series: Materials Science and Engineering* 258:012007. <https://doi.org/10.1088/1757-899x/258/1/012007>

- [41] Simonelli M, McCartney DG, Barriobero-Vila P, Aboulkhair NT, Tse YY, Clare A, Hague R (2020) The Influence of Iron in Minimizing the Microstructural Anisotropy of Ti-6Al-4V Produced by Laser Powder-Bed Fusion. *Metall and Mat Trans A* 51(5):2444-2459. <https://doi.org/10.1007/s11661-020-05692-6>
- [42] Ghosh A, Modak P, Dutta R, Chakrabarti D (2016) Effect of MnS inclusion and crystallographic texture on anisotropy in Charpy impact toughness of low carbon ferritic steel. *Materials Science and Engineering: A* 654:298-308. <https://doi.org/10.1016/j.msea.2015.12.047>
- [43] Bermingham MJ, McDonald SD, Dargusch MS (2018) Effect of trace lanthanum hexaboride and boron additions on microstructure, tensile properties and anisotropy of Ti-6Al-4V produced by additive manufacturing. *Materials Science and Engineering: A* 719:1-11. <https://doi.org/10.1016/j.msea.2018.02.012>
- [44] Saylor DM, El-Dasher BS, Adams BL, Rohrer GS (2004) Measuring the five-parameter grain-boundary distribution from observations of planar sections. *Metall and Mat Trans A* 35(7):1981-1989.
- [45] Rohrer GS (2011) Grain boundary energy anisotropy: a review. *J Mater Sci* 46(18):5881-5895. <https://doi.org/10.1007/s10853-011-5677-3>
- [46] Adams BL, Field DP (1992) Measurement and representation of grain-boundary texture. *MTA* 23(9):2501-2513.
- [47] Randle V (2004) Twinning-related grain boundary engineering. *Acta materialia* 52(14):4067-4081.
- [48] Watanabe T, Tsurekawa S (1999) The control of brittleness and development of desirable mechanical properties in polycrystalline systems by grain boundary engineering. *Acta Materialia* 47(15):4171-4185. [https://doi.org/10.1016/S1359-6454\(99\)00275-X](https://doi.org/10.1016/S1359-6454(99)00275-X)
- [49] Watanabe T (2011) Grain boundary engineering: historical perspective and future prospects. *J Mater Sci* 46(12):4095-4115. <https://doi.org/10.1007/s10853-011-5393-z>
- [50] Schuh CA, Kumar M, King WE (2003) Analysis of grain boundary networks and their evolution during grain boundary engineering. *Acta Materialia* 51(3):687-700.
- [51] Laleh M, Hughes AE, Tan MY, Rohrer GS, Primig S, Haghdadi N (2021) Grain boundary character distribution in an additively manufactured austenitic stainless steel. *Scripta Materialia* 192:115-119. <https://doi.org/10.1016/j.scriptamat.2020.10.018>
- [52] Fang XY, Li HQ, Wang M, Li C, Guo YB (2018) Characterization of texture and grain boundary character distributions of selective laser melted Inconel 625 alloy. *Materials Characterization* 143:182-190. <https://doi.org/10.1016/j.matchar.2018.02.008>
- [53] Holland S, Wang X, Fang XY, Guo YB, Yan F, Li L (2018) Grain boundary network evolution in Inconel 718 from selective laser melting to heat treatment. *Materials Science and Engineering: A* 725:406-418. <https://doi.org/10.1016/j.msea.2018.04.045>
- [54] Segura IA, Murr LE, Terrazas CA, Bermudez D, Mireles J, Injeti VSV, Li K, Yu B, Misra RDK, Wicker RB (2019) Grain boundary and microstructure engineering of Inconel 690 cladding on stainless-steel 316L using electron-beam

- powder bed fusion additive manufacturing. *Journal of Materials Science & Technology* 35(2):351-367. <https://doi.org/10.1016/j.jmst.2018.09.059>
- [55] Ronneberg T, Davies CM, Hooper PA (2020) Revealing relationships between porosity, microstructure and mechanical properties of laser powder bed fusion 316L stainless steel through heat treatment. *Materials & Design* 189:108481. <https://doi.org/10.1016/j.matdes.2020.108481>
- [56] RG Prasad M, Biswas A, Geenen K, Amin W, Gao S, Lian J, Röttger A, Vajragupta N, Hartmaier A (2020) Influence of Pore Characteristics on Anisotropic Mechanical Behavior of Laser Powder Bed Fusion–Manufactured Metal by Micromechanical Modeling. *Advanced Engineering Materials*:2000641.
- [57] Yadroitsev I, Krakhmalev P, Yadroitsava I (2014) Selective laser melting of Ti6Al4V alloy for biomedical applications: Temperature monitoring and microstructural evolution. *Journal of Alloys and Compounds* 583:404-409. <https://doi.org/10.1016/j.jallcom.2013.08.183>
- [58] Shifeng W, Shuai L, Qingsong W, Yan C, Sheng Z, Yusheng S (2014) Effect of molten pool boundaries on the mechanical properties of selective laser melting parts. *Journal of Materials Processing Technology* 214(11):2660-2667. <https://doi.org/10.1016/j.jmatprotec.2014.06.002>
- [59] Rosenthal I (2019) Microstructure and Mechanical Properties of AlSi10Mg Components Produced by the Laser Beam Additive Manufacturing (AM) Technology. (Ben Gurion University of the Negev, Beersheba, Israel).
- [60] Rosenthal I, Stern A, Frage N (2017) Strain rate sensitivity and fracture mechanism of AlSi10Mg parts produced by Selective Laser Melting. *Materials Science and Engineering: A* 682:509-517. <https://doi.org/10.1016/j.msea.2016.11.070>
- [61] Xiong ZH, Liu SL, Li SF, Shi Y, Yang YF, Misra RDK (2019) Role of melt pool boundary condition in determining the mechanical properties of selective laser melting AlSi10Mg alloy. *Materials Science and Engineering: A* 740-741:148-156. <https://doi.org/10.1016/j.msea.2018.10.083>
- [62] Bartlett JL, Li X (2019) An overview of residual stresses in metal powder bed fusion. *Additive Manufacturing* 27:131-149. <https://doi.org/10.1016/j.addma.2019.02.020>
- [63] Li C, Liu ZY, Fang XY, Guo YB (2018) Residual Stress in Metal Additive Manufacturing. *Procedia CIRP* 71:348-353. <https://doi.org/10.1016/j.procir.2018.05.039>